

Marangoni flow driven hysteresis and azimuthal symmetry breaking in evaporating binary droplets

Duarte Rocha¹†, Detlef Lohse^{1,2}‡, and Christian Diddens¹¶

¹Physics of Fluids Department, Max-Planck Center Twente for Complex Fluid Dynamics and J. M. Burgers Centre for Fluid Dynamics, University of Twente, P. O. Box 217, 7500AE Enschede, The Netherlands

²Max-Planck Institute for Dynamics and Self-Organization, Am Faßberg 17, 37077 Göttingen, Germany

(Received xx; revised xx; accepted xx)

The non-uniform evaporation rate at the liquid-gas interface of binary droplets induces solutal Marangoni flows. In glycerol-water mixtures (positive Marangoni number, where the *more* volatile fluid has higher surface tension), these flows stabilise into steady patterns. Conversely, in water-ethanol mixtures (negative Marangoni number, where the *less* volatile fluid has higher surface tension), Marangoni instabilities emerge, producing seemingly chaotic flows. This behaviour arises from the opposing signs of the Marangoni number. Perturbations locally reducing surface tension at the interface drive Marangoni flows away from the perturbed region. Incompressibility enforces a return flow, drawing fluid from the bulk towards the interface. In mixtures with a negative Marangoni number, preferential evaporation of the lower-surface-tension component leads to a higher concentration of the higher-surface-tension component at the interface as compared to the bulk. The return flow therefore creates a positive feedback loop, further reducing surface tension in the perturbed region and enhancing the instability. This study investigates bistable quasi-stationary solutions in evaporating binary droplets with negative Marangoni numbers (e.g. water-ethanol) and examines symmetry breaking across a range of Marangoni number and contact angles. Bistable regions exhibit hysteresis. Remarkably, flat droplets (small contact angles) show instabilities at much lower critical Marangoni numbers than droplets with larger contact angles. Our numerical simulations reveal that interactions between droplet height profiles and non-uniform evaporation rates trigger azimuthal Marangoni instabilities in flat droplets. This geometrically confined instability can even destabilise mixtures with positive Marangoni numbers, particularly for concave liquid-gas interfaces. Finally, through Lyapunov exponent analysis, we confirm the chaotic nature of flows in droplets with a negative Marangoni number.

Key words:

† Email address for correspondence: d.rocha@utwente.nl

‡ Email address for correspondence: d.lohse@utwente.nl

¶ Email address for correspondence: c.diddens@utwente.nl

1. Introduction

The flow dynamics within evaporating sessile droplets are critical in controlling deposition patterns, which are highly significant for numerous industrial applications such as biological deposition methods (Dugas *et al.* 2005), spray cooling (Kim 2007) or inkjet printing (Lohse 2022). In the simplest case of a single-component droplet evaporating under ambient conditions, the evaporation rate is typically non-uniform along the liquid-gas interface, as long as the contact angle (θ) differs from exactly 90° (Deegan *et al.* 1997, 2000; Popov 2005). This position-dependent evaporation rate induces capillary flows. The best known of such case is the one with a pinned contact line, often referred to as the “coffee-stain effect” (Deegan *et al.* 1997, 2000). In that case, the mass loss, in the region of higher evaporation, namely at the rim (for droplets with contact angle lower than 90°), is compensated by a flow towards the rim, while the shape of the droplet remains a spherical-cap.

In cases where evaporative cooling is significant, surface tension gradients arise due to temperature variations at the liquid-gas interface, leading to thermal Marangoni flows that can even overcome the “coffee-stain effect” (Hu & Larson 2006). These flows are driven by thermal gradients. In contrast, concentration differences in evaporating *multicomponent* droplets trigger solutal Marangoni flows, which are usually considerably stronger. In fact, Thomson (1855) famously first described this phenomenon in the “tears of wine” effect, where the faster evaporation of ethanol at the contact line in a wine cup (essentially water-ethanol) results in concentration gradients, driving the upward movement of fluid along the glass. As a result, droplets are formed and grow, ultimately falling due to gravity, and leading to the “tears of wine” (Loewenthal 1931; Hosoi & Bush 2001).

Water-ethanol mixtures, in particular, display a variety of fascinating phenomena (see review of Lohse & Zhang (2020) for a general understanding of physicochemical hydrodynamics of multicomponent systems). Among these, there is interfacial instability, which manifests as seemingly chaotic flows with erratic asymmetric convection rolls, driven by either (or both) thermal and solutal gradients. Initial observations of interfacial instabilities by Bénard (1901) were interpreted as natural convection, but Pearson (1958) analytically demonstrated that surface tension gradients could also explain some of those instabilities. Sternling *et al.* (1959) investigated the nature of the solutal Marangoni effect in detail and demonstrated that the direction of the concentration gradient in bulk direction, as well as the viscosity and diffusivity ratios between both phases, are key factors for the dynamics.

Interestingly, while these instabilities occur in water-ethanol mixtures, they do not manifest in glycerol-water systems (Diddens *et al.* 2021). The key difference between these two systems is the sign of the Marangoni number (Ma) (Gelderblom *et al.* 2022). This difference can be understood by considering two two-dimensional boxes with periodic side boundaries and an evaporating top surface: one containing a glycerol-water mixture (figure 1(a)) and the other containing a water-ethanol mixture (figure 1(b)). In the glycerol-water system, which has a positive Marangoni number, evaporation of the more volatile component (water) increases the concentration of the fluid with low surface tension (glycerol) at the interface. Conversely, in the water-ethanol system, which has a negative Marangoni number, evaporation of the more volatile component (ethanol) increases the concentration of the fluid with high surface tension (water) at the interface. If a perturbation locally reduces surface tension at the interface, it generates a Marangoni flow away from the perturbed region (middle frames in figure 1). Incompressibility enforces a return flow from the bulk to the perturbed region to compensate for the

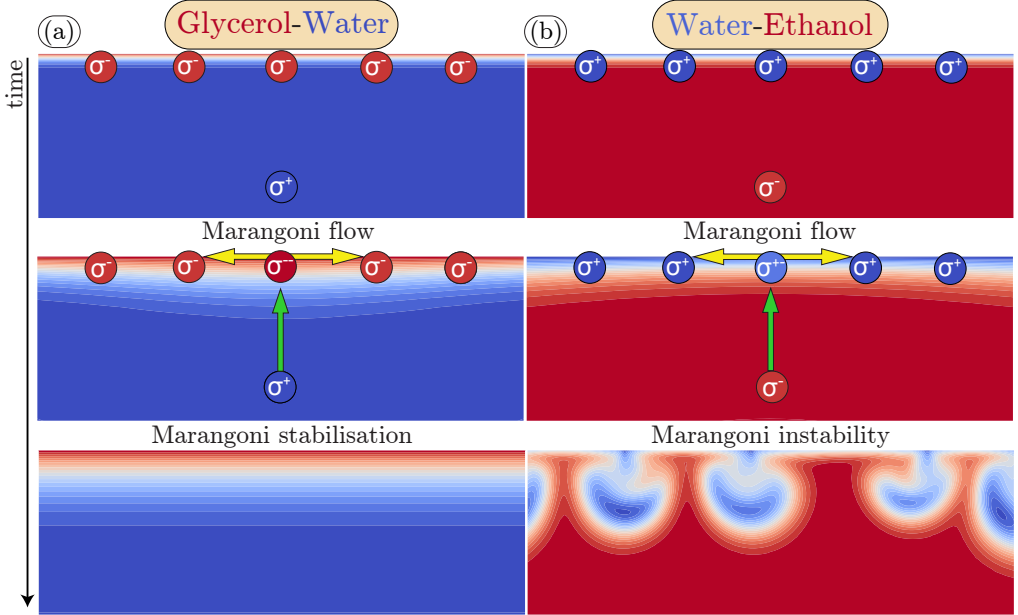


FIGURE 1. Schematic representation of the onset of Marangoni stabilisation (a) and instability (b) in a two-dimensional box with periodic boundaries and with an evaporating top surface, containing a glycerol-water mixture (a) and a water-ethanol mixture (b). In (a), due to water being more volatile than glycerol, the surface tension at the interface is reduced as compared to the bulk. In (b), vice-versa, due to the higher volatility of ethanol, the surface tension at the interface is enhanced as compared to the bulk. A disturbance that locally diminishes surface tension at the interface generates a Marangoni flow directed away from the disturbed area. Incompressibility generates a return flow from the bulk to the disturbed region. In the glycerol-water mixture, this return flow transports liquid with higher surface tension into the disturbed area, thereby mitigating the Marangoni flow. Conversely, in the water-ethanol mixture, the return flow carries liquid with lower surface tension into the disturbed area, further reducing the surface tension and amplifying the Marangoni flow. Consequently, a positive feedback loop of Marangoni and return flows is established, resulting in the Marangoni instability.

displaced liquid. In the system with a positive Marangoni number, the return flow brings liquid with higher surface tension into the perturbed region, damping the Marangoni flow. In contrast, in the system with a negative Marangoni number, the return flow brings liquid with lower surface tension into the perturbed region, further decreasing the surface tension and enhancing the Marangoni flow. As a result, a positive feedback of Marangoni and return flows is created, leading to the fascinating flow patterns known as Marangoni instability (lower frame in figure 1(b)).

We emphasise that return flow from the bulk towards the interface plays a crucial role in amplifying Marangoni instabilities in this system. While the former explanation generally applies to geometries where bulk return flow can develop, in e.g. a Hele-Shaw cell (Linde *et al.* 1964; De La Cruz *et al.* 2021), the influence of alternative geometries on the onset of instabilities remains an open question. Droplets have a three-dimensional curved droplet-gas interface, leading to more intricate solutal (and thermal) Marangoni flows compared to simpler geometries, thereby resulting in interesting flows as a product of the complex interaction of its multiple components, see e.g. Rowan *et al.* (2000); Sefiane *et al.* (2008); Tan *et al.* (2016); He & Qiu (2016); Diddens *et al.* (2017b); Wang *et al.* (2022); Lohse (2022). Mixtures with negative Marangoni number exhibit violent flows with larger fluctuations in the early stages, while the concentration of the most volatile

component is high, eventually relaxing to a capillary flow when this concentration reduces to a minimal value (Christy *et al.* 2011; Bennacer & Sefiane 2014). Marangoni instabilities have also been observed in pure ethanol droplets evaporating in a humid environment, where the instabilities were associated with the adsorption of water in the droplet during evaporation (Shin *et al.* 2016; Fukatani *et al.* 2016; Kita *et al.* 2018; Yang *et al.* 2023). To further complicate the evaporative process, in the later stages of evaporation, the droplet can adopt a pancake-like shape (Diddens *et al.* 2017a; Pahlavan *et al.* 2021; Yang *et al.* 2023), where the droplet-gas interface deforms due to Marangoni stresses. For flat droplets, one might naively assume that the absence of bulk would inhibit the onset of Marangoni instabilities. However, previous studies have documented the occurrence of vigorous convective rolls even in small contact angle water-ethanol droplets (e.g. Christy *et al.* 2011).

In this study, we employ a minimal model to investigate the flow regimes in quasi-stationary evaporating droplets with negative Marangoni number as a function of the Marangoni number Ma and the contact angle θ , initially under the assumption of axisymmetry. We then analyse the azimuthal stability of these solutions for different azimuthal wavenumbers m , revealing that flat droplets are more susceptible to instabilities compared to those with larger contact angle θ . We utilise a simplified lubrication model to provide scaling arguments, based on the droplet height profile, to justify the emergence of instabilities at low critical Ma number particularly for droplets with low θ . Additionally, we show that, counterintuitively, evaporating glycerol-water mixtures can exhibit Marangoni instabilities when put in a shallow well, illustrating a strong geometric influence on the mechanism of the Marangoni instability. Throughout this work, in our numerical models, we neglect transient effects. We consider that only one liquid phase evaporates (Popov 2005). We disregard effects of Raoult's law. We neglect the slow motion of the interface compared to the Marangoni convection. We assume a perfect spherical-cap droplet shape. All of these approximations may limit the applicability of the model to real systems. Our primary aim is to isolate the fundamental mechanisms driving the onset of Marangoni instabilities and provide a quantitative analysis of the flow stability, which can be refined in future studies to account for more complex and realistic conditions. The influence of droplet deformation on our results is briefly discussed. Finally, we compute Lyapunov exponents to demonstrate the chaotic nature of these flows using lubrication theory with two lateral dimensions.

The paper is structured as follows: In §2.1, we introduce the equations used to explore flow regimes in evaporating droplets with negative Marangoni effects, and we introduce the control parameters. This is followed by an analysis of quasi-stationary solutions at θ close to 90° as a function of Ma in §2.2 and the identification of different flow regimes across the full Ma - θ phase space in §2.3. The azimuthal stability of the quasi-stationary regimes is studied in §3.1 and §3.2. In §4.1, we introduce the simplified lubrication model, which is then used to explain the onset of azimuthal instabilities in flat droplets in §4.2. In §4.3, we propose a well geometry for glycerol-water mixtures exhibiting Marangoni instabilities. The influence of droplet deformation is discussed in §4.4. In §5, we compute Lyapunov exponents to illustrate the chaotic behaviour of these flows. The paper ends with the conclusion and outlook (§6).

2. Onset of instability

2.1. Full model and its control parameters

The evaporation of binary droplets is a complex multi-physics problem that involves interfacial mass transfer. This phenomenon has been successfully analysed numerically using transient (Diddens *et al.* 2017b) and quasi-stationary models (Diddens *et al.* 2021). In this study, we examine the stability of quasi-stationary flow solutions within binary droplets, with focus on Marangoni instabilities occurring when the most volatile component has the lower surface tension, as briefly described in this section.

When modelling the evolution of each component α in the liquid phase, it is sufficient to track the mass fraction y_A of the more volatile component A , considering that $y_A + y_B = 1$. Typically, the liquid's velocity \mathbf{u} is much larger than the interface velocity \mathbf{u}_I (Diddens *et al.* 2021). This results in minimal compositional variations in the liquid phase during the drying process, making it reasonable to express y_A as $y_A = y_{A,0} + y$, where $y_{A,0}$ is the spatially averaged composition and y is a small perturbation.

The composition-dependent liquid properties can then be approximated using a first-order Taylor expansion around $y_{A,0}$. We neglect the dependence of the liquid's properties on temperature on the basis that its variations are small compared to the changes in composition. While variations in the liquid density can influence the flow pattern within binary droplets (Edwards *et al.* 2018; Li *et al.* 2019; Diddens *et al.* 2021), this effect is neglected in the present study for simplicity, in order to focus instead on pure Marangoni-induced flows. The droplet is assumed to perfectly form a spherical-cap shape throughout the calculations in this section, implying that the capillary (and Bond) number(s) are effectively zero. The contact angle with the substrate is called θ . All material properties are assumed to be constant regardless of the composition (and temperature), except for the liquid-gas surface tension, given by $\sigma(y_A) = \sigma(y_{A,0}) + y\partial_{y_A}\sigma$. We introduce non-dimensionalised scales (marked with tildes) for space, time, velocity, and pressure:

$$x = V^{1/3}\tilde{x}, \quad t = \frac{V^{2/3}}{D_0}\tilde{t}, \quad \mathbf{u} = \frac{D_0}{V^{1/3}}\tilde{\mathbf{u}}, \quad p = \frac{\mu_0 D_0}{V^{2/3}}\tilde{p},$$

where V is the volume of the droplet and D_0 is the diffusion coefficient evaluated at the average composition $y_{A,0}$. Similarly, one can obtain the non-dimensionalised gas concentration \tilde{c} , whose profile around the droplet determines the evaporation rate of each component, assuming the droplet evaporates under ambient conditions (Deegan *et al.* 1997, 2000; Popov 2005). By neglecting the dependencies of the vapour concentration on the composition, one can write

$$\tilde{c} = (c_\alpha - c_\alpha^\infty)/(c_\alpha^{\text{eq}} - c_\alpha^\infty), \quad (2.1)$$

where c_α^∞ is the ambient vapour concentration far from the droplet and $c_\alpha^{\text{eq}} = c_\alpha^{\text{pure}}\gamma_\alpha x_\alpha$, as given by Raoult's law. Here, c_α^{pure} is the saturation concentration of the pure component α at its average composition, γ_α is the activity coefficient, and x_α is the liquid mole fraction. For simplicity, the saturation concentration c_α^{eq} is assumed to be constant. Following this scaling, $\tilde{c} = 1$ at the liquid-gas interface and $\tilde{c} = 0$ far from the droplet. As originally validated by Deegan *et al.* (2000) and Hu & Larson (2002) for pure liquids and by Diddens (2017) for multicomponent droplets, the solution of the Laplace equation

$$\nabla^2 \tilde{c} = 0 \quad (2.2)$$

in the gas phase gives \tilde{c} . Disregarding Stefan flow (Brutin & Starov 2018), the dimensionless evaporation rate j_α is given by the diffusive mass flux

$$\tilde{j} = -\tilde{\partial}_n \tilde{c}, \quad (2.3)$$

which induces variations in the liquid composition through the flux boundary condition

$$-\nabla y \cdot \mathbf{n} = \text{Ev} \tilde{j}. \quad (2.4)$$

Here, Ev is the evaporation number, which measures the strength of the concentration gradient created in the liquid due to the preferential evaporation of one of the components, defined as (Diddens *et al.* 2021)

$$\text{Ev} = \frac{(1 - y_{A,0})D_A^{\text{vap}}(c_{A,0}^{\text{eq}} - c_A^\infty) - y_{A,0}D_B^{\text{vap}}(c_{B,0}^{\text{eq}} - c_B^\infty)}{\rho_0 D_0},$$

In the liquid phase, the conservation of mass and momentum is described by the following Stokes equations, respectively given by

$$\tilde{\nabla} \cdot \tilde{\mathbf{u}} = 0, \quad (2.5)$$

$$-\tilde{\nabla} \tilde{p} + \tilde{\nabla}^2 \tilde{\mathbf{u}} = 0, \quad (2.6)$$

where gravity is neglected for simplicity. For convenience, we define the modified mass fraction variations $\xi = y/\text{Ev}$, which allows us to reduce the number of control parameters of the problem. When substituting $y = \text{Ev}\xi$ in equation (2.4), the liquid-gas interface boundary condition becomes

$$-\nabla \xi \cdot \mathbf{n} = \tilde{j}. \quad (2.7)$$

Since the diffusion coefficient in the liquid phase is typically small, we consider the full convection-diffusion equation for the variations of mass fraction ξ

$$\partial_t \xi + \tilde{\mathbf{u}} \cdot \tilde{\nabla} \xi = \tilde{\nabla}^2 \xi, \quad (2.8)$$

Equation (2.8) contains the only relevant transient term that can affect the stability of this system, since the small Schmidt number indicates that velocity is “enslaved” to compositional gradients. The interface is subject to Marangoni stresses:

$$\mathbf{n} \cdot (\tilde{\nabla} \tilde{\mathbf{u}} + (\tilde{\nabla} \tilde{\mathbf{u}})^t) \cdot \mathbf{t} = \text{Ma} \tilde{\nabla}_t \xi \cdot \mathbf{t}, \quad (2.9)$$

where $\tilde{\nabla}_t$ represents the surface gradient operator. The Marangoni number Ma is defined as

$$\text{Ma} = \frac{V^{1/3} \partial_{y_A} \sigma}{D_0 \mu_0} \text{Ev},$$

and μ_0 is the dynamic viscosity evaluated at the average composition $y_{A,0}$.

We consider a spherical-cap for the droplet shape (i.e. capillary number $\text{Ca} \rightarrow 0$) and since $\mathbf{u}_I \ll \mathbf{u}$, we enforce $\tilde{\mathbf{u}} \cdot \mathbf{n} = 0$ by a normal traction. At the substrate, a no-slip boundary condition is imposed, i.e. $\tilde{\mathbf{u}} = 0$, and the Neumann boundary condition $\nabla \xi \cdot \mathbf{n} = 0$ is applied to prevent normal mass flux through the substrate. To eliminate the null space of the pressure field, an average pressure constraint is imposed, i.e., $\int \tilde{p} dV = 0$. This is enforced numerically via a Lagrange multiplier. Similarly, a zero-average constraint is imposed to remove the constant shift for ξ .

The system of equations is solved using a finite element method implemented in the software package PYOOMPH[†] (Diddens & Rocha 2024), which is based on OOMPH-LIB (Heil & Hazel 2006) and GiNAC (Bauer *et al.* 2002). All domains are discretised on an axisymmetric mesh with triangular elements. Linear basis functions are used for ξ and \tilde{p} , while quadratic basis functions are employed for the $\tilde{\mathbf{u}}$ field. Initially, the system is solved to obtain the quasi-stationary solution for the flow and composition fields within the droplet. The stability of this solution is then assessed by examining the eigenvalues

[†] Available at: <https://pyoomph.github.io/>

using a shift-inverted Arnoldi method. If any bifurcation is detected by analysing the eigenvalues, bifurcation tracking as outlined by [Diddens & Rocha \(2024\)](#) is used to locate the bifurcation curve as function of the contact angle.

2.2. Instabilities close to $\theta = 90^\circ$

In the limit of zero capillary number, there are two control parameters in the problem of this study: Ma and the contact angle θ . For glycerol-water mixtures, where Ma is positive, the quasi-stationary solutions for the flow and composition fields within the droplet are stable, unique, axisymmetric, and not subject to hysteresis for all θ ([Diddens *et al.* 2021](#)). Exactly at $\theta = 90^\circ$, \tilde{j} is uniform along the liquid-gas interface, resulting in a diffusive profile for ξ and absence of flow within the droplet. On hydrophilic substrates, i.e. forming contact angles $\theta < 90^\circ$, the larger evaporation rate at the contact line reduces the surface tension locally, inducing a Marangoni flow from the contact line towards the top of the droplet. On hydrophobic substrates, i.e. forming contact angles $\theta > 90^\circ$, the Marangoni flow is in the opposite direction, since the evaporation rate is larger at the top of the droplet.

In contrast, water-ethanol mixtures, where Ma is negative, exhibit much more complex behaviour. Strong transient effects and asymmetric, seemingly chaotic flows have been reported both experimentally ([Machrafi *et al.* \(2010\)](#); [Diddens *et al.* \(2017b\)](#)) and numerically ([Diddens *et al.* \(2017b\)](#)). Here, we examine the stationary solutions at negative Marangoni numbers Ma with an initially small modulus, before the onset of these instabilities, and gradually decrease Ma to more negative numbers while monitoring the linear stability of the solutions.

At exactly $\theta = 90^\circ$, we observe a purely diffusive profile for ξ , but this solution is only stable at sufficiently low $|Ma|$. Here, a non-zero Rayleigh number (Ra), i.e. buoyant forces, would initiate flow, but we emphasise again that our analysis here is for $Ra = 0$, i.e. negligible density contrasts. Above the critical $|Ma|$ value, $-Ma > -Ma_{cr} \approx 167$, multiple solution branches coexist (see phase portrait in [Figure 2b](#)). Depending on the initial conditions, the flow can develop either a vortex from the apex to the rim (A→R), a vortex from the rim to the apex (R→A), or two competing vortices (2V). At Ma_{cr} , the flow field's symmetry is broken in an imperfect pitchfork bifurcation (see e.g. [Golubitsky & Schaeffer \(1979\)](#); [Strogatz \(2018\)](#)), corresponding to the normal form $\dot{x} = rx + hx^2 - x^3$, where r is the control parameter and h the imperfection parameter. If $h = 0$, we would retrieve a perfect pitchfork bifurcation. In other words, the diffusive profile becomes unstable through a transcritical bifurcation, where it exchanges stability with the R→A solution branch, while the A→R branch loses stability via a fold bifurcation at a slightly lower Ma (see inset in [figure 2\(b\)](#)). Our numerical tests suggest that the no-slip boundary condition at the substrate and the axisymmetric coordinate system disrupt the physical symmetry that would otherwise be present, leading to the imperfect pitchfork bifurcation. At higher $|Ma|$, the R→A, 2V, and A→R solution branches each lose stability through either a fold or a Hopf bifurcation.

For slightly lower θ , e.g. $\theta = 89^\circ$, the diffusive state no longer exists and the flow exhibits a A→R solution for low $|Ma|$. Despite the induced Marangoni flow pushing the fluid from the top towards the contact line (i.e. in the A→R direction), a R→A solution can still be found, which shows strong hysteresis. The stability of these solutions is limited by fold bifurcations at different Ma (see [figure 2a](#)). For slightly larger θ , e.g. $\theta = 91^\circ$, the flow exhibits a R→A solution for low $|Ma|$. Curiously, this solution branch loses its stability in a fold bifurcation at a lower $|Ma|$ than its A→R counterpart for the same set of parameters (see [figure 2c](#)), which can again be attributed to the three-dimensional geometry and the presence of the no-slip condition. While Marangoni flow pushes the

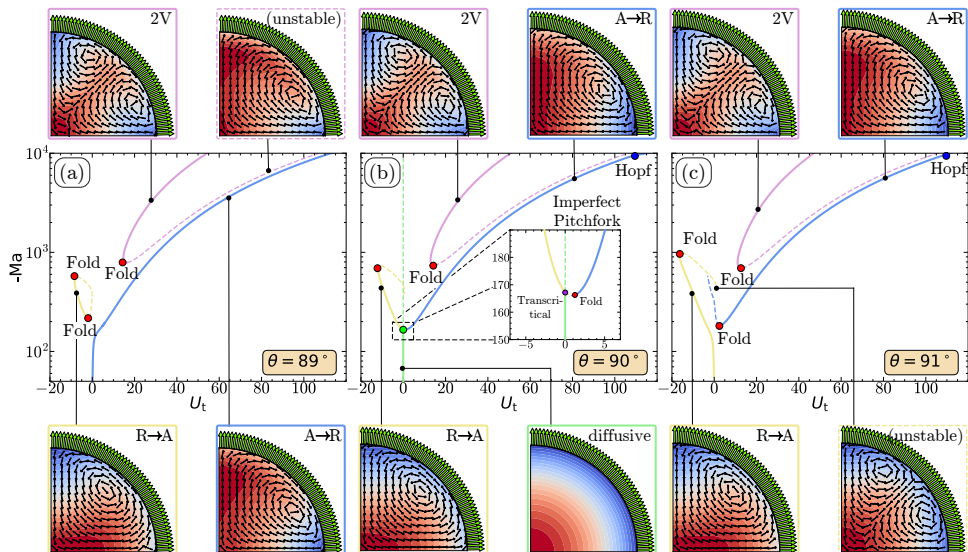


FIGURE 2. Phase portrait of solution branches as a function of Ma , for $\theta = 89^\circ$ (a), $\theta = 90^\circ$ (b), and $\theta = 91^\circ$ (c). The x -axis represents the average tangential velocity at the liquid-gas interface, a key measure of the flow field, indicating the flow direction within the droplet when a single vortex is present. The flow field and ξ profile for selected $A \rightarrow R$, $R \rightarrow A$, and $2V$ solutions are also depicted. Here, the diverging blue to red colours in the contour plots represent increasing ξ of the fluid with the lowest surface tension, e.g. ethanol in water-ethanol mixtures. At $\theta = 90^\circ$, the ξ profile is purely diffusive for low Ma , becoming unstable at a critical Ma_{cr} in an imperfect Pitchfork bifurcation (green). The inset in (b) shows the $\theta = 90^\circ$ phase portrait in a range of Ma from 150 to 190, where the imperfect Pitchfork is clearly visible. All other solution branches lose their stability in either fold (red) or a Hopf (blue) bifurcations.

fluid from the contact line towards the top of the droplet (i.e. in the $R \rightarrow A$ direction), a $A \rightarrow R$ solution presents, counter-intuitively, for large enough Ma , better stability than the $R \rightarrow A$ one.

This intriguing introduction to the vast array of bistable solutions within the narrow Ma - θ phase space investigated here sets the stage for the topic to be discussed in the following subsection, which covers the stability of the quasi-stationary solutions on an extensive Ma - θ phase diagram.

2.3. Ma vs θ phase diagram

In this section, we utilise the bifurcation tracking tool outlined by [Diddens & Rocha \(2024\)](#). Building upon the initial findings from the preceding subsection, we employ arclength continuation on θ to trace the bifurcation curves along the Ma - θ phase diagram. Arclength continuation on θ requires remeshing the domain whenever the grid deformation surpasses a certain threshold. We used highly refined meshes near the liquid-gas interface, with a total of $\sim 40\,000$ degrees of freedom, to accurately capture the Marangoni flow. The curves in figure 3 remained unchanged with further grid refinement, confirming mesh independence.

We find a complex bifurcation diagram where multiple solution branches coexist across a broad spectrum of Ma and θ values (figure 3). This diagram is segmented into three distinct regimes, each representing stable quasi-stationary axisymmetric $A \rightarrow R$, $2V$ or $R \rightarrow A$ solutions (blue, plum and yellow colours, respectively). Transitions between these regimes are characterised by fold or Hopf bifurcations, indicating shifts in the stability

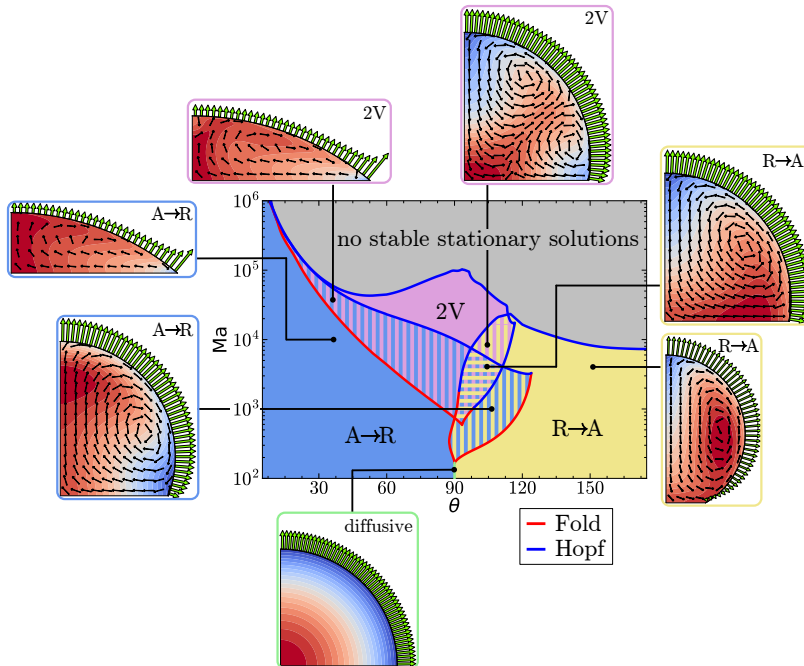


FIGURE 3. Bifurcation diagram of the quasi-stationary axisymmetric solutions as a function of Ma and θ . The diagram is divided into three regimes, where the stable solutions are either a $A \rightarrow R$ solution (blue colour), a $R \rightarrow A$ solution (yellow colour), or a $2V$ solution (plum colour). The transition between these regimes is marked by fold (red) or Hopf (blue) bifurcations. Above the upper Hopf bifurcation curves, no stable quasi-stationary solutions are found (gray).

of solution branches. By calculating the oscillation amplitude A of the *rms*-velocity of transient oscillatory solutions near selected Hopf bifurcations, we observe that these ultimately reach a stable limit cycle, $A \sim \sqrt{Ma - Ma_{cr}}$. This allows us to classify these Hopf bifurcations as supercritical. Under the assumptions and flow conditions of this subsection, we have not observed any subcritical Hopf bifurcations.

The lack of stable quasi-stationary solutions beyond the upper Hopf bifurcation curves is worth noting. Here, nonlinearity governs the flow field, eventually leading to seemingly chaotic behaviour as observed experimentally and numerically in previous studies (Machrafi *et al.* (2010); Diddens *et al.* (2017b)). Interestingly, the bifurcations diagram is overlaid with a network of bistable regions. In these areas, the flow field can display solutions from different regimes depending on initial conditions, thereby demonstrating significant hysteresis.

The calculated set of solutions provides a comprehensive overview of the stability of the quasi-stationary axisymmetric solutions within binary droplets with negative Ma . However, the azimuthal stability of these solutions has not yet been addressed in this section, which is the focus of the following sections.

3. Azimuthal stability

We employ the method detailed in Diddens & Rocha (2024) to explore the phenomenon of axisymmetric breaking across the $R \rightarrow A$, $2V$ and $A \rightarrow R$ solution regimes. We determine the stability of the quasi-stationary axisymmetric base solutions for specific azimuthal

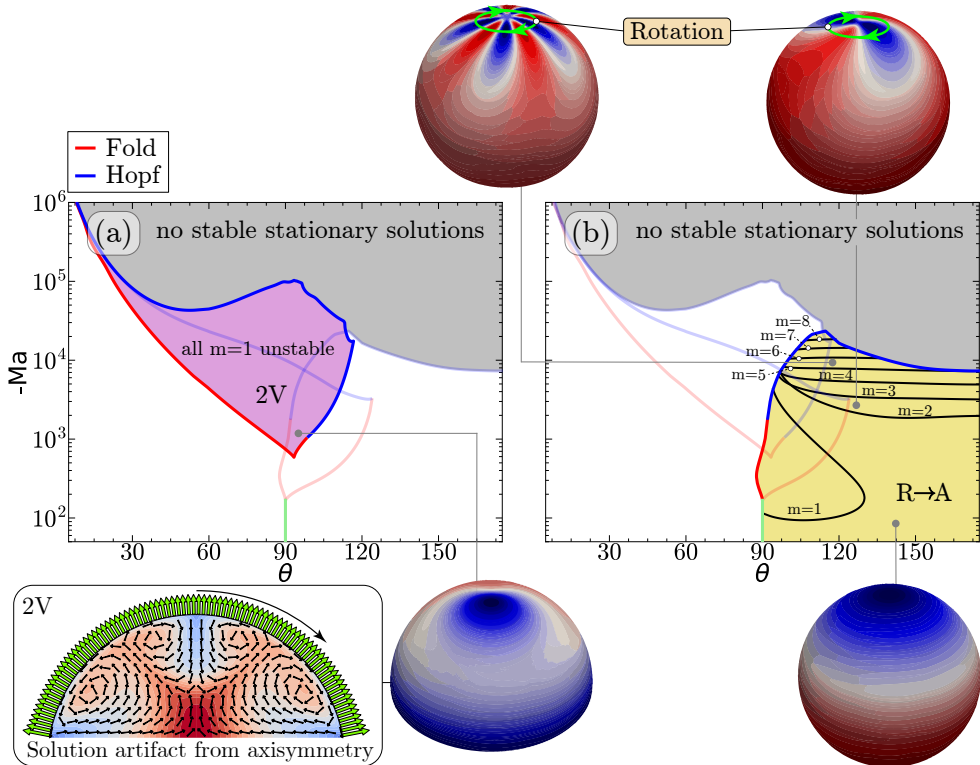


FIGURE 4. Azimuthal bifurcation diagram for the stability of the quasi-stationary axisymmetric solutions in the 2V (a) and R→A (b) solutions regimes. In (a), the bifurcations that limit the stability of the A→R and R→A solution regimes are shown with lower opacity. Similarly, in (b), the bifurcations for the A→R and 2V solutions are depicted with lower opacity (see all curves in figure 3). In the 2V regime, all base solutions are unstable for $m = 1$, leading to a single vortex, as depicted at the bottom right of (a). The 2V regime is therefore interpreted as an artifact of the imposed axisymmetry in §2.3, where the upper vortex merges with its counterpart in the rim region of the droplet, as depicted at the bottom left of (a). In the R→A regime, multiple bifurcations are observed corresponding to the instability of modes $m = 1$ to $m = 8$. The adjacent plots show an isometric view of an azimuthally stable solution (bottom right), and solutions subject to the linear effects of $m = 2$ (top right), and $m = 5$ (top left) azimuthally unstable perturbations. Exclusively in the R→A regime, the eigenvalues and eigenfunction had a non-zero imaginary part, indicating rotational motion, as depicted by the green arrows in the two upper plots.

wavenumbers m , i.e. the stability of perturbations $\propto \exp(im\phi)$, where ϕ is the azimuthal coordinate.

3.1. Regimes with vortices from rim to apex or with two vortices

We first focus on the 2V regime (figure 4a). All of these base solutions exhibit an instability for $m = 1$. Such instability can be interpreted as the merging of the upper vortex with its counterpart in the rim region of the droplet, resulting in a single vortex (as depicted in the bottom of figure 4a). Consequently, the 2V flow field is merely an artifact of the imposed axisymmetry during the computation of the base solutions.

In contrast, the R→A vortex regime (see figure 4b) presents a variety of bifurcations, along with a stable axisymmetric regime (e.g. at $\theta = 140^\circ$ and $-\text{Ma} = 100$, as shown in the bottom right of figure 4b). For lower θ within this regime, a $m = 1$ bifurcation at

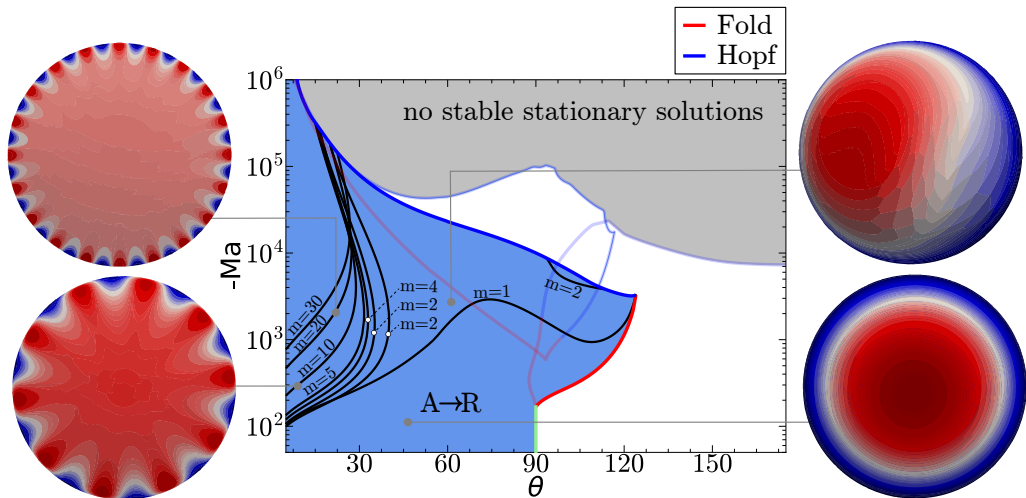


FIGURE 5. Azimuthal bifurcation diagram assessing the stability of the quasi-stationary axisymmetric solutions in the A→R regime. The bifurcations that limit the stability of the 2V and R→A solution regimes are shown with lower opacity (see all curves in figure 3). The bifurcation curves depict the range from $m = 1$ to $m = 30$. The adjacent plots show a top view of the droplet in a stable axisymmetric regime (bottom right) or subject to the linear effects of $m = 1$ (top right), 10 (bottom left), and 20 (top left) unstable perturbations on the azimuthal instability.

a relatively low $-Ma_{cr} \sim 100$ breaks the axisymmetry. Interestingly, the axisymmetric stability can be regained by sufficiently increasing $|Ma|$. However, if $|Ma|$ continues to rise, the base solution becomes unstable for $m = 2$, and subsequently for $m = 3$ up to $m = 8$. As $|Ma|$ exceeds the critical value for each bifurcation, the axisymmetry can be disrupted in a corresponding mode m , as depicted in the adjacent plots of figure 4b. These plots are derived by expanding the ξ field into a sum of the base solution and a small amplitude perturbation in the direction of the corresponding eigenvector that triggers the instability of mode m . While in the long-term limit the resulting ξ profile will be governed by nonlinear coupling of additional excited modes, we only represent the linear effects of each mode to offer a clear visualisation of the azimuthal instability. We highlight the presence of a non-zero imaginary part in the eigenvalue and eigenfunction of the velocity field for the R→A regime, indicating rotational motion in the perturbed flow field, as depicted by the green arrows in the top plots. This result is consistent with the reports of [Babor & Kuhlmann \(2023\)](#) for thermal Marangoni flow in sessile droplets.

3.2. Regime with vortex from apex to rim

In the regime of the A→R solution, we observe multiple bifurcations for various m values (see figure 5). For larger θ , greater than 45° , the axisymmetric base solution remains stable for $|Ma|$ values below a critical $m = 1$ bifurcation (see adjacent plot at the bottom right of figure 5), while it becomes unstable for $m = 1$ above this bifurcation (see adjacent plot at the top right of figure 5). Additionally, there exists a narrow region where certain combinations of Ma and θ lead to a $m = 2$ unstable solution. This region is observed for θ values slightly above 90° and $Ma \sim -10^4$.

For lower θ , we observe a multitude of bifurcations, as illustrated in figure 5, ranging from $m = 1$ to 30 (instabilities with $m > 30$ are not indicated in figure 5). The bottom and top left adjacent plots provide representations for $m = 10$ and 20, respectively.

Interestingly, the critical Marangoni number Ma_{cr} for the onset of all instabilities is particularly low for smaller θ . This observation contradicts the explanation given for Marangoni instabilities in a two-dimensional box in section §1. In a two-dimensional box, the instabilities are driven by a positive feedback loop, where a perturbation locally reduces surface tension at the interface, inducing a Marangoni flow. This, in turn, generates a return flow in the bulk, drawing more fluid with low surface tension towards the perturbed region. However, in the case of flat droplets (i.e. small θ), the bulk domain becomes so shallow that vertical diffusion averages out any considerable compositional gradients in height direction, consistent with the assumptions of lubrication theory. Thus, the vertical return flow is absent, breaking the positive feedback loop. Contrary to expectations that Marangoni instabilities would be suppressed for low θ values, we observe the opposite behaviour.

To deeply understand this intriguing occurrence, we introduce a lubrication model in the following section. This model reduces the number of parameters to one, namely just a Marangoni number. In the limit of small θ , the contact angle can be absorbed in the nondimensionalisation.

4. Instabilities for low contact angle θ

4.1. Lubrication model and its control parameter

In the limit of small θ , the vertical gradients are negligible compared to the radial or azimuthal ones. Rather than solving the full axisymmetric equations, we can then simplify the problem by applying lubrication theory. This allows us to simply consider a one-dimensional grid using a polar coordinate system. Alternatively, a two-dimensional circular mesh could be used, taking a Cartesian coordinate system, albeit with an increased computational cost. We choose the first option in this section.

In the lubrication approximation of an evaporating droplet (Eggers & Pismen 2010; Diddens *et al.* 2017a), the governing equations for the pressure p , height profile h and vertically averaged mass fraction y_A are given by, assuming a lateral flow profile parabolic in height direction:

$$\partial_t h = -\nabla \cdot \mathbf{Q} - \frac{j}{\rho}, \quad (4.1)$$

$$p + \nabla \cdot (\sigma \nabla h) = 0, \quad (4.2)$$

$$\partial_t (h y_A) + \nabla \cdot (\mathbf{Q} y_A) = \nabla \cdot (D h \nabla y_A) - \frac{j_A}{\rho}, \quad (4.3)$$

$$\mathbf{Q} = -\frac{h^3}{3\mu} \nabla p + \frac{h^2}{2\mu} \nabla \sigma, \quad (4.4)$$

Note that the transient effects are more pronounced for flat droplets as compared to droplets with higher contact angle. However, we calculate the quasi-stationary solutions of the lubrication model for simplicity. We assume that the evaporation of one component is balanced by the condensation of the other in the quasi-stationary limit, such that the total volume remains constant. Thereby, we consider the evaporation rate j_A to be given by the theoretically calculated limit for a flat pure droplet (Popov 2005),

$$j_A = \frac{2D_A^{\text{vap}}(c_A^{\text{eq}} - c_A^\infty)}{\pi\sqrt{1-r^2}}. \quad (4.5)$$

As in §2.1, we assume that the droplet maintains its initial shape, i.e. we consider the limit of zero capillary number $\text{Ca} = 0$ and $\partial_t h = 0$. In the limit of the lubrication

theory, the equilibrium shape corresponds to a parabolic height profile. We emphasise that these approximations may limit the applicability of the results in real systems, but they capture the essential physics that explain the onset of the Marangoni instability. By reformulating $\xi = y\theta/Ev$ and applying the mentioned assumptions, while using the nondimensional scales introduced in §2.1 – but now modifying the length scale to the base radius R instead of $V^{1/3}$ – we can reduce the system of equations (4.1)–(4.4) to:

$$\tilde{\nabla} \cdot \tilde{\mathbf{Q}} = 0, \quad (4.6)$$

$$\tilde{\nabla} \cdot (\tilde{\mathbf{Q}}\xi) = \tilde{\nabla} \cdot (\tilde{h}\tilde{\nabla}\xi) - \tilde{j}, \quad (4.7)$$

$$\tilde{\mathbf{Q}} = -\frac{\tilde{h}^3}{3}\tilde{\nabla}\tilde{p} + \text{Ma}_R\frac{\tilde{h}^2}{2}\tilde{\nabla}\xi. \quad (4.8)$$

Here, $\tilde{h} = 0.5(1 - \tilde{x}^2)$ is the dimensionless height profile, $\tilde{j} = 2/(\pi\sqrt{1 - r^2})$ is the evaporation rate in the flat droplet limit and Ma_R is the modified Marangoni number, defined as:

$$\text{Ma}_R = \frac{R\partial_{y_A}\sigma}{D_0\mu_0}E_V,$$

We impose a homogeneous bulk correction for ξ , i.e., $\langle \xi \rangle = 0$, to allow for quasi-stationary solutions with a fixed compositional average. While the system of equations (4.6)–(4.8) can be solved analytically (see Appendix A), introducing a small amplitude ϵ of an azimuthal perturbation to the base solution makes the augmented system too complex for analytical solutions. Therefore, we employ numerical methods to determine the azimuthal stability of the quasi-stationary axisymmetric solutions and compare these results with those obtained using the full model described in §2.1. As $\theta \rightarrow 0$, the results from the full model converge to the lubrication model, validating the latter (see figure 6b). Remarkably, the number of unstable modes m is found to be consistent in both models. Interestingly, this number is larger for low θ values than for large θ values (see figure 6a), i.e. a cascade of azimuthal instabilities sets in for decreasing θ at unexpectedly small negative Marangoni numbers. By expanding the ξ field into a sum of the base solution and a small amplitude perturbation in the direction of the corresponding eigenvector that triggers the instability of mode m , we can visualise the linear effects of the azimuthal instability for the lubrication model.

4.2. Driving mechanism of the azimuthal instabilities

In the absence of bulk gradients, the driving mechanism of the Marangoni instabilities for low θ values is different from the one described in the two-dimensional box of §1, yet it bears resemblance.

For droplets with small θ and a negative Marangoni number (Ma_R), the larger evaporation rate at the contact line leads to an enhanced concentration of fluid with greater surface tension. Should a disturbance locally reduce the surface tension at contact line, it triggers an azimuthal Marangoni flow that transports fluid away from the perturbed region. Incompressibility initiates a pressure-driven return flow, which attracts more fluid with lower surface tension towards the contact line (see figure 7). This creates a positive feedback loop, which is the driving mechanism of the azimuthal instabilities observed in droplets with low contact angle θ .

Naturally, the same reasoning still holds for droplets with larger contact angle θ . However, in this latter case, the presence of bulk gradients becomes more pronounced, primarily driving the Marangoni instabilities. A simple observation of the scaling of the different terms in equation (4.8) reveals that the flow induced by Ma_R scales with h^2 ,

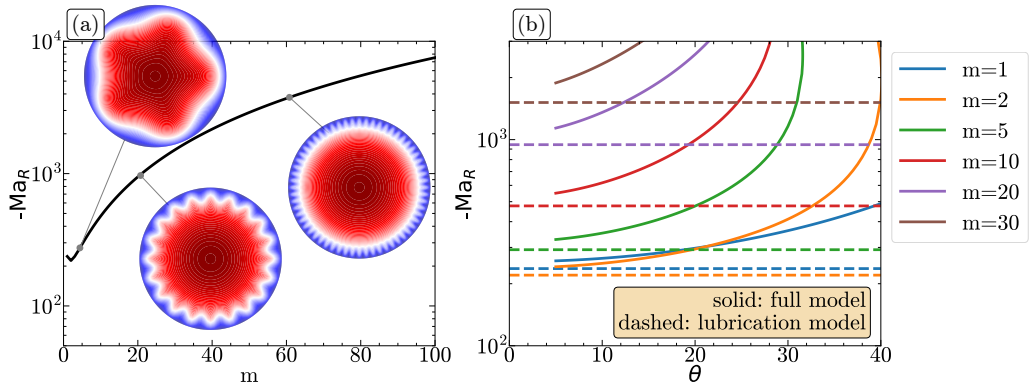


FIGURE 6. (a) Onset of azimuthal instabilities for different m as a function of Ma_R in the limit of small θ . The adjacent plots show a top view of the droplet subject to the linear effects $m = 5$ (top left), $m = 20$ (bottom left), and $m = 60$ (bottom right) unstable perturbations on the azimuthal instability. (b) Comparison of the azimuthal stability of the quasi-stationary axisymmetric solutions between the full model as $\theta \rightarrow 0$ (solid) and the lubrication model (dashed).

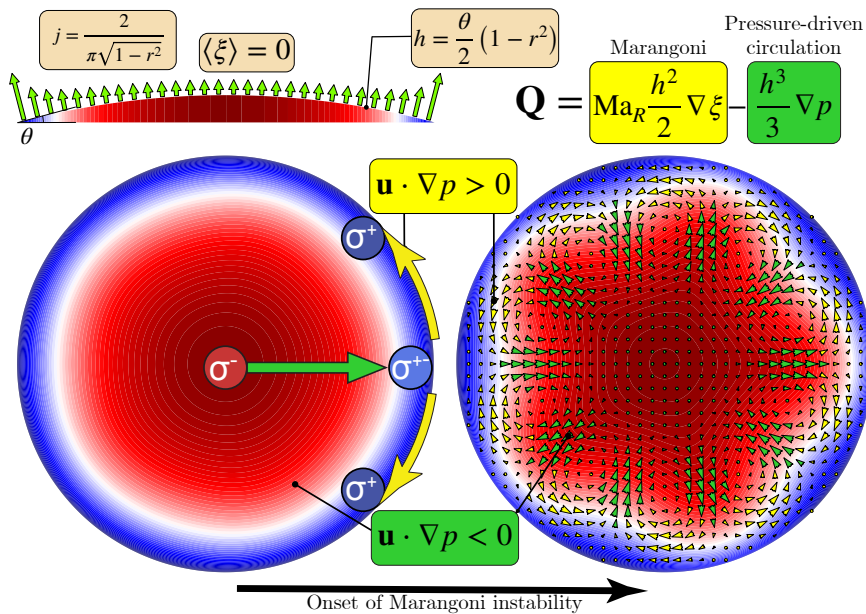


FIGURE 7. Side (left top) and top (left bottom) views of an evaporating droplet prior to the onset of the Marangoni instability. Should a disturbance locally reduce the surface tension at the contact line, it triggers an azimuthal Marangoni flow (yellow arrows) that transports fluid away from the perturbed region. This initiates pressure-driven return flow (green arrow) that attracts more fluid with lower surface tension from the centre of the droplet (greater-height region) towards the contact line (lower-height region). Ultimately, an azimuthal Marangoni instability is triggered (right).

while the flow driven by pressure scales with h^3 . As a consequence, in areas where the height profile is minimal, the Marangoni flow prevails, but in areas with a significant height profile, pressure-driven flow takes precedence. Thus, in droplets with a low θ , the

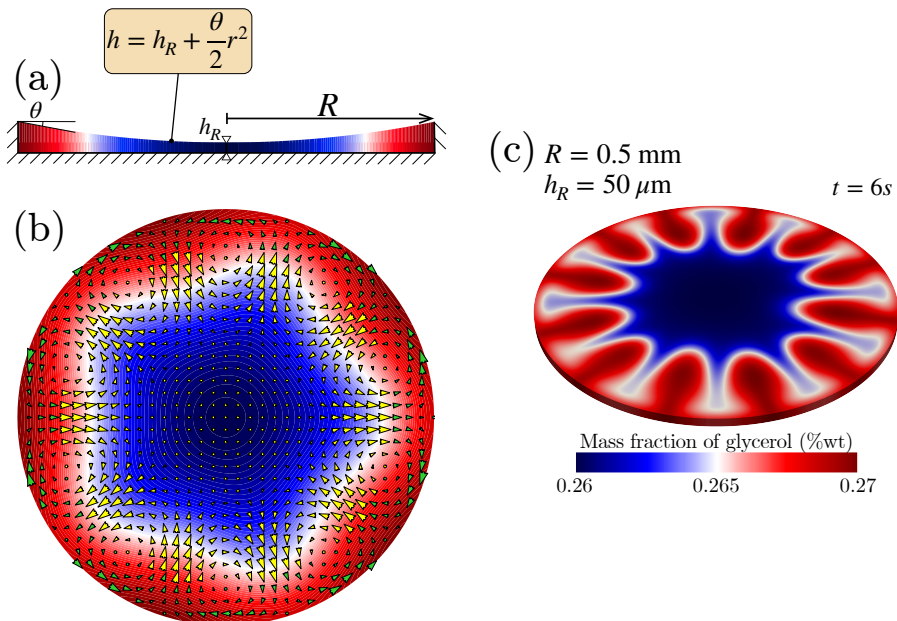


FIGURE 8. Side (a) and top (b) views of a droplet placed on a shallow pit. Due to the inverted height profile, Ma_R (yellow arrows) is predominant at the centre over the pressure-driven flow (green arrows), resulting in the onset of azimuthal Marangoni instabilities, depicted in (b). After enough evaporation time (6 s), blobs emerge close to the contact line in realistic case of a $R = 0.5$ mm, $\theta = 10^\circ$, positive- Ma_R droplet in a $h_R = 0.5$ μ m pit, with initial $y_{\text{glycerol}} = 25\%$ (c).

flow near the contact line is predominantly driven by Marangoni flow, whereas pressure-driven circulation dominates the centre (as illustrated by the arrows in figure 7).

Therefore, the geometry plays a fundamental role in the driving mechanism of the onset of azimuthal instabilities. In the next subsection, we propose a geometry where such instabilities can be obtained for positive- Ma_R droplets (e.g. glycerol-water mixtures).

4.3. Instabilities in positive Marangoni mixtures

The insights gained from prior analyses elucidate that, in droplets with small θ , if the fluid with larger surface tension has the lowest height profile, azimuthal instabilities can be triggered. For positive- Ma_R mixtures, the enhanced evaporation at the contact line leads to higher surface tension in the centre, which is the zone of larger height. Thereby, positive- Ma_R mixtures consistently exhibit stable axisymmetric solutions. Any disturbance reducing the surface tension at the centre is promptly neutralised by a Marangoni flow in the opposite direction.

Altering the scenario by placing the droplet within a shallow pit with a concave liquid-gas interface reverses the height profile, making the centre the lowest point (see figure 8a). This setup assumes that the depression is shallow enough for lubrication theory to hold and that the fluid remains pinned to the pit's sidewalls. Under these conditions, a perturbation reducing surface tension at the centre instigates a Marangoni flow that shifts fluid azimuthally away from the disturbed area, thereby initiating an azimuthal Marangoni instability akin to the mechanism described in §4.2, albeit in a reversed direction (see figure 8b). This behaviour is unexpected when following the explanation provided in §1 for Marangoni instabilities in a two-dimensional box. In that scenario, positive- Ma mixtures cannot initiate Marangoni instabilities.

To simulate the evaporation dynamics of a realistic glycerol-water droplet with a radius of $R = 0.5 \text{ mm}$, $\theta = 10^\circ$, in a pit of depth $h_R = 0.5 \text{ }\mu\text{m}$, starting with a $y_{\text{glycerol}} = 25 \%$, we apply equations (4.1)–(4.4) in a two-dimensional circular domain. As evaporation progresses, blobs begin to form near the rim of the well due to the azimuthal Marangoni instability (see figure 8c). We emphasise that the pit must be shallow enough for the onset of instabilities, otherwise bulk gradients would stabilise the flow. While this finding is remarkable, a detailed investigation of the azimuthal Marangoni dynamics of droplets in such a well is beyond the scope of the work.

4.4. Capillary effects in the Marangoni instability

Until now, we assumed that the droplet retains a perfectly spherical-cap shape (parabolic shape in the lubrication limit) during evaporation, neglecting capillary effects on the onset of instabilities. In this subsection, we explore non-zero capillary numbers to examine the influence of capillary effects on the onset of azimuthal instabilities. Utilising the scaling introduced in §4.1 and defining the capillary number as:

$$\text{Ca} = \frac{D_0 \mu_0}{R \sigma_0},$$

we can obtain the nondimensionalised form of equations (4.1)–(4.4), namely

$$\partial_{\tilde{t}} \tilde{h} + \tilde{\nabla} \cdot \tilde{\mathbf{Q}} = 0, \quad (4.9)$$

$$\tilde{p} + \tilde{\nabla} \cdot \left((\text{Ca}^{-1} + \text{Ma}_R \xi) \tilde{\nabla} \tilde{h} \right) = 0, \quad (4.10)$$

$$\partial_{\tilde{t}} (\xi \tilde{h}) + \tilde{\nabla} \cdot (\tilde{\mathbf{Q}} \xi) = \tilde{\nabla} \cdot (\tilde{h} \tilde{\nabla} \xi) - \tilde{j}, \quad (4.11)$$

The definition of $\tilde{\mathbf{Q}}$ remains the same as in equation (4.8). Again, we neglect the “coffee-stain effect” in equation (4.9), in the sense that we assume that the volume of the droplet does not change. By solving the system of equations (4.9)–(4.11) for various capillary numbers, we can identify the critical Ma_R for the onset of azimuthal instabilities across different wavenumbers m (see figure 9) and understand how the results of figure 6 are affected by shape deformations. We ensure that the capillary number Ca is set such that the surface tension, given in equation (4.10) by $\sigma = \text{Ca}^{-1} + \text{Ma}_R \xi$, remains positive. Beyond this limit, we discard the solutions as they are physically unrealistic, as depicted by the gray area of figure 9, limited by the black dashed line.

The results indicate that within the physical constraints of the capillary number (Ca), the critical Marangoni number (Ma_R) for the onset of azimuthal instabilities is only marginally affected by shape deformations. However, it is important to note that pancake-shaped droplets have been observed both experimentally and numerically (Diddens *et al.* 2017a; Pahlavan *et al.* 2021; Yang *et al.* 2023), which stands in contrast to our findings where the droplet is hardly deformed within the physical limits. We reiterate that our approach is a simplified representation of the real system, and the results should be interpreted with caution, since we focus primarily on the mechanisms driving the onset of azimuthal instabilities in the framework of a minimal model.

A slight increase in the modulus of the critical Marangoni number is observed across all azimuthal wavenumbers m , with a more pronounced effect for $m = 1$, where $|\text{Ma}_R|$ increases from approximately 230 to 300 as Ca rises from 0 to around 0.01. In evaporating droplets with positive Marangoni number and with unpinned contact line, the Marangoni flow can drive fluid towards the apex strongly enough to contract the droplet (“Marangoni contraction”, Karpitschka *et al.* 2017). Similarly, a pinned droplet with negative Marangoni number can form a pancake-shape (Pahlavan *et al.* 2021; Yang *et al.*

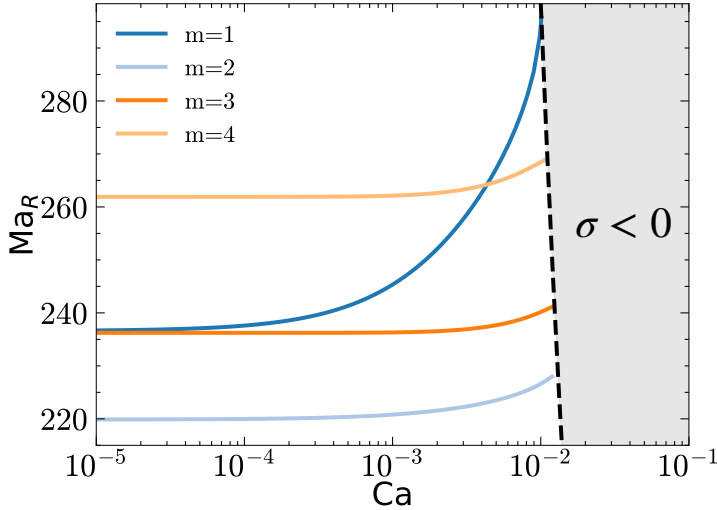


FIGURE 9. Critical Marangoni number (Ma_R) for the onset of azimuthal instabilities as a function of the capillary number Ca for wavenumbers $m = 1, 2, 3$ and 4 . The gray area, limited by the black dashed line, indicates where the surface tension is negative, rendering physically unrealistic solutions, therefore discarded from the analysis.

2023), where strong Marangoni flow drives fluid from the apex of the droplet towards the contact line, causing deformation and an increase in the height profile at the contact line. As a result, the Marangoni forces at the contact line are weakened, necessitating a higher $|\text{Ma}_R|$ for the onset of azimuthal instabilities. Despite this, the overall influence of Ca on the critical Marangoni number remains minimal, supporting the assumption, under the simplifications made, that the droplet retains a nearly spherical-cap shape during evaporation.

5. Chaotic behaviour of negative Marangoni evaporating droplet

Until this section, we carefully characterised the observed flow as “seemingly” chaotic. Here, we utilise the zero- Ca lubrication model from §4.1 within a circular domain to accurately capture the radial and azimuthal flow features of flat droplets, i.e. the full nonlinear long-term behaviour beyond the onset of instability. Our objective is to characterise the complex spatio-temporal dynamics of flat evaporating droplets with negative Ma_R , specifically to determine whether the system exhibits chaotic behaviour.

In a chaotic system, small changes in the initial conditions exponentially grow in time. In dissipative systems, the distance between two phase space trajectories with slightly different initial conditions remains bounded within a strange attractor (Strogatz 2018). To investigate this dynamical system, we monitor the evolution of a small perturbation $\mathbf{U}(t) + \delta\mathbf{U}(t)$ relative to the unperturbed solution $\mathbf{U}(t)$, under the assumption that both will eventually converge to the same strange attractor. We analyse the linear growth of $\delta\mathbf{U}(t)$ around $\mathbf{U}(t)$. Despite the system’s nonlinearities, the long-term dynamics are expected to exhibit exponential growth or decay, represented as $\delta\mathbf{U}(t) \sim e^{\lambda t}$, provided that δU stays tiny, i.e. nonlinear terms do not take action yet. In an N -dimensional dynamical system, there are typically N Lyapunov exponents λ_i , with $i = 1, \dots, N$ (Strogatz 2018). If at least one of these exponents is positive, it indicates that a random perturbation will generally grow over time, signifying chaotic behaviour.

To calculate the Lyapunov exponents, we start with one or more initial random

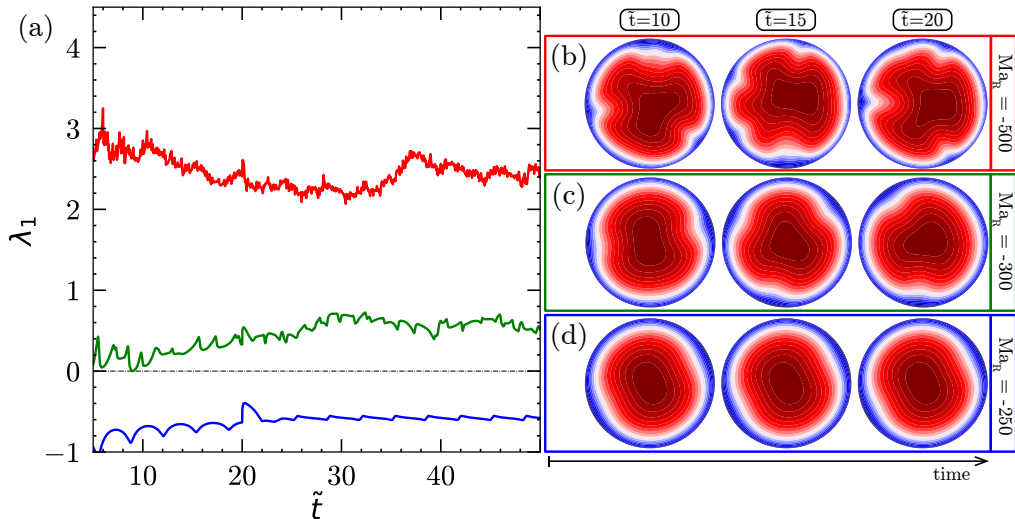


FIGURE 10. Largest Lyapunov exponent for $\text{Ma}_R = -500$ (red), $\text{Ma}_R = -300$ (green), and $\text{Ma}_R = -250$ (blue) (a), plotted over dimensionless time \tilde{t} . The black dotted line indicates the transition to chaotic behaviour, i.e. when the largest Lyapunov exponent becomes positive. The ξ profile at $\tilde{t} = 10, 15$, and 20 for $\text{Ma}_R = -500$ (b), $\text{Ma}_R = -300$ (c), and $\text{Ma}_R = -250$ (d).

perturbations $\delta\mathbf{U}_i(0)$, for $i \leq N$. Here, N is the number of degrees of freedom of the discretised composition ξ , which contains the only time derivative. If $i > 1$, we perform Gram-Schmidt orthogonalization (Wiesel 1993; Christiansen & Rugh 1997) at each step to ensure that slower-growing perturbations remain orthogonal to the fastest-growing ones. The Lyapunov exponents are then determined from their definition

$$\lambda_i = \lim_{\tilde{t} \rightarrow \infty} \lim_{|\delta\mathbf{U}_i^0| \rightarrow 0} \frac{1}{\tilde{t}} \log \frac{|\delta\mathbf{U}_i(\tilde{t})|}{|\delta\mathbf{U}_i^0|}. \quad (5.1)$$

In practice, however, we calculate the exponential growth over a finite dimensionless averaging time \tilde{t} , since the infinite time limit cannot be realised in numerical calculations. We use $\tilde{t} = \min(\tilde{t}, 20)$ to bypass the initial transient dynamics of the evaporative process, which would otherwise skew the Lyapunov exponent calculations and necessitate computationally more expensive simulations.

To avoid a completely transient system, we consider a droplet with a fixed volume V and a constant average concentration field $\langle \xi \rangle$. Although this assumption may not be entirely realistic during the temporal evolution of an evaporating flat droplet, our goal is to provide insights into the deterministic nature of the flow field within the droplet at a specific time when the droplet has a defined volume and average concentration.

For both $\text{Ma}_R = -500$ and $\text{Ma}_R = -300$, the largest Lyapunov exponent is positive, as shown by the red and green curves in figure 10(a). The ξ profile changes significantly over time, displaying irregular and aperiodic patterns, as seen in figures 10(b) and (c). Our calculations indicate that higher $|\text{Ma}_R|$ values result in more pronounced chaotic behaviour, evidenced by larger Lyapunov exponents. When $|\text{Ma}_R|$ is reduced to 250, the largest Lyapunov exponent becomes negative, as shown by the blue curve in figure 10(a). The solutions appear to stabilise over time, as illustrated in figure 10(d), and a dominant $m = 2$ -unstable mode is observed in the resulting quasi-stationary ξ profile.

For a critical $|\text{Ma}_R|$ between 250 and 300, the largest Lyapunov exponent approaches zero, indicating a transition to chaotic behaviour. By applying the linear stability analysis

method outlined in §2.1 to the quasi-stationary solutions of the two-dimensional system in the lubrication limit, we can pinpoint the critical Ma_R at which this transition occurs. We identify a subcritical Hopf bifurcation at $\text{Ma}_R = -268.69$, signalling the onset of chaotic dynamics and limiting the system’s deterministic behaviour. This relatively low critical Ma_R value aligns with experimental observations of violent and random flow fields in evaporating droplets with negative Ma_R (Machrafi *et al.* 2010; Diddens *et al.* 2017b). For instance, a water-ethanol droplet with a 1 mm radius, a 10° contact angle, and 10 wt% ethanol, evaporating at ambient conditions and relative humidity of 50 %, can easily reach an order of magnitude $\text{Ma}_R \sim -10^7$. Our findings confirm that these observations are indicative of chaotic nonlinear behaviour rather than merely the superposition of linearly unstable modes.

6. Conclusions

Evaporating multicomponent droplets with a negative Marangoni number (e.g. water-ethanol droplets) can exhibit interfacial instabilities (Pearson 1958; Sternling *et al.* 1959). These instabilities arise due to the sign of the solutal Marangoni number, i.e. whether surface tension increases or decreases with the mass fraction of the most volatile component (Gelderblom *et al.* 2022). In the latter case, as the most volatile component evaporates, surface tension becomes greater at the liquid-gas interface compared to the surface tension corresponding to the liquid composition in the bulk. Any perturbation that locally reduces the surface tension at the interface, will trigger a Marangoni flow that transports fluid away from the disturbed region. In a sufficiently thick bulk domain, continuity forms a vertical return flow, enhancing the perturbation by drawing more fluid with low surface tension towards the perturbed region. Remarkably, our calculations reveal that the onset of instabilities occurs at a much lower critical $|\text{Ma}_{\text{cr}}|$ for droplets with low θ than for droplets with a more significant bulk domain.

To investigate this phenomenon, we first identified the quasi-stationary axisymmetric solution regimes — vortex from rim to apex (R→A), vortex from apex to rim (A→R), and two vortices (2V) — near $\theta = 90^\circ$ as a function of Ma , and subsequently explored the full Ma - θ phase space using a minimal model. We then assessed the azimuthal stability of each regime individually. In the R→A regime, the axisymmetric solution remains stable for $|\text{Ma}|$ values below a critical $m = 1$ bifurcation but becomes unstable for $m = 1$ above this threshold. By further increasing $|\text{Ma}|$, more bifurcation curves for different m values are crossed – up to $m = 8$. All quasi-stationary solutions in the 2V regime were $m = 1$ -unstable. The A→R regime revealed a multitude of bifurcations for droplets with too low contact angle θ , with several unstable modes m , contradicting the intuitive expectation that Marangoni instabilities would be suppressed – or at least reduced – in the absence of a thick bulk domain.

We then applied a simplified lubrication model to explore the onset of azimuthal instabilities in the small θ limit. Although we derived an analytical axisymmetric solution, the perturbed fields were too complex to be solved analytically, leading us to employ numerical methods to uncover the mechanism driving these instabilities. We found that the higher evaporation rate at the contact line enhances the concentration of fluid with higher surface tension. A disturbance locally reducing surface tension at the contact line initiates an azimuthal Marangoni flow, which removes fluid from the perturbed region and triggers a pressure-driven azimuthal return flow. This flow attracts more low-surface-tension fluid towards the contact line, creating a positive feedback loop that drives the instabilities. By analysing the scales of the Marangoni (h^2) and pressure-driven (h^3) flows in equation (4.8), we demonstrated that the droplet’s height profile

plays a crucial role in the onset of these instabilities. If the region of lowest height coincides with the highest surface tension, azimuthal instabilities can occur. Thereby, placing a glycerol-water droplet in a shallow pit, reversing the height profile, can induce such instabilities, opposed to a glycerol-water droplet on a flat substrate, which does show azimuthal instabilities. This finding stresses the importance of the geometry on the interfacial instabilities.

It is important to note that these results were obtained using a minimal model in which the droplet was assumed to retain a spherical-cap shape during evaporation – an assumption that may not hold in real systems (Diddens *et al.* 2017a; Pahlavan *et al.* 2021; Yang *et al.* 2023). We also investigated the influence of non-zero capillary numbers on the onset of azimuthal instabilities. The results suggest that, while the critical Ma_R for azimuthal instabilities is only marginally affected by shape deformations, our simplified approach requires caution when interpreting these findings. Lastly, we explored the chaotic behaviour of evaporating droplets with negative Ma_R using a two-dimensional lubrication model. We determined that the critical $Ma_R = -268.69$ marks the onset of chaotic dynamics, which aligns with experimental observations of violent flow fields in such droplets.

In conclusion, we have presented a detailed analysis of the onset of azimuthal instabilities in evaporating droplets with negative Ma_R number. By isolating the solutal Marangoni effects, we demonstrated that these instabilities can occur even when thermal effects are neglected. Our results highlight the fundamental role of the height profile in driving instabilities for flat droplets. Additionally, we showed that the chaotic flows observed in evaporating droplets with negative Ma_R are due to inherent chaotic dynamics rather than the superposition of linearly unstable modes.

This work opens new avenues for further research, such as investigating the evaporation of droplets with positive Marangoni number in shallow pits, which could extend the work of D’Ambrosio *et al.* (2023). Incorporating more complex effects, such as a comprehensive evaporation model or “coffee-stain flow”, could provide a more realistic representation of the system and facilitate direct comparisons with experimental results. Also, secondary bifurcations could be identified and Lyapunov exponents for high contact angle droplets could be extracted from full three-dimensional simulations. This, however, constitutes a numerically expensive and demanding task.

From a broader perspective, our analysis demonstrates (i) how incredibly rich the flow regimes of evaporating binary droplets is and (ii) that nevertheless, it is, at least in part and with justified approximations, accessible to mathematical analysis.

Declaration of Interests

The authors report no conflict of interest.

Acknowledgements

This work was supported by an Industrial Partnership Programme, High Tech Systems and Materials (HTSM), of the Netherlands Organisation for Scientific Research (NWO); a funding for public-private partnerships (PPS) of the Netherlands Enterprise Agency (RVO) and the Ministry of Economic Affairs (EZ); Canon Production Printing Netherlands B.V.; and the University of Twente.

Appendix A. Analytical axisymmetric solution in lubrication limit and zero-Ca

The system of equations (4.6) to (4.8) can be solved analytically for the quasi-stationary axisymmetric base solution in the limit of small θ and zero capillary number. The existence of an axisymmetric flow requires the absence of z-averaged velocity, or equivalently, $\mathbf{Q}^0 = 0$. Here, the tilde was omitted for simplicity and the superscript 0 denotes the axisymmetric base solution. In consequence, there will be no net advective transport of the composition, which simplifies equation (4.7) to a Poisson equation with a source term (j). The analytical solution can thus be expressed as:

$$\mathbf{Q}^0 = 0, \quad (\text{A1})$$

$$\xi^0 = \frac{-6r^2 + 12 \operatorname{artanh}(\sqrt{1-r^2}) + 12 \log(r) - 5}{3\pi\theta}, \quad (\text{A2})$$

$$p^0 = \frac{12\text{Ma}_R}{\pi\theta^2} \left(\frac{1}{\sqrt{1-r^2}} - \log(1 + \sqrt{1-r^2}) \right), \quad (\text{A3})$$

where r is the radial coordinate in the axisymmetric coordinate system. Despite the presence of a logarithm in the ξ^0 solution, it remains well-defined at $r = 0$. This is due to the log-singularity being counterbalanced by the equivalent divergence of artanh . However, as anticipated, the pressure exhibits a divergence at the contact line when the Marangoni number is non-zero.

When we introduce a small amplitude ϵ perturbation to expand each field f into $f = f^0 + \epsilon f^m e^{im\phi + \lambda t}$, the simplification of $\mathbf{Q} = 0$ no longer applies. This is because the divergence of the expanded \mathbf{Q} field is no longer zero. As a result, the advective transport of the composition is non-zero, yielding complex analytical expressions for the perturbed fields. Given these complexities, it was not possible to derive an analytical solution for the perturbed fields in the lubrication limit.

REFERENCES

- BABOR, L. & KUHLMANN, H. C. 2023 Linear stability of thermocapillary flow in a droplet attached to a hot or cold substrate. *Phys. Rev. Fluids* **8** (11), 114003.
- BAUER, C. , FRINK, A. & KRECKEL, R. 2002 Introduction to the GiNaC framework for symbolic computation within the C++ programming language. *J. Symb. Comput.* **33** (1), 1–12.
- BÉNARD, H. 1901 *Les tourbillons cellulaires dans une nappe liquide propageant de la chaleur par convection, en régime permanent*. Gauthier-Villars.
- BENNACER, R. & SEFIANE, K. 2014 Vortices, dissipation and flow transition in volatile binary drops. *J. Fluid Mech.* **749**, 649–665.
- BRUTIN, D. & STAROV, V. 2018 Recent advances in droplet wetting and evaporation. *Chem. Soc. Rev.* **47** (2), 558–585.
- CHRISTIANSEN, F. & RUGH, H. H. 1997 Computing Lyapunov spectra with continuous Gram-Schmidt orthonormalization. *Nonlinearity* **10** (5), 1063.
- CHRISTY, J. R. , HAMAMOTO, Y. & SEFIANE, K. 2011 Flow transition within an evaporating binary mixture sessile drop. *Phys. Rev. Lett.* **106** (20), 205701.
- D’AMBROSIO, H.-M. , WILSON, S. K. , WRAY, A. W. & DUFFY, B. R. 2023 The effect of the spatial variation of the evaporative flux on the deposition from a thin sessile droplet. *J. Fluid Mech.* **970**, A1.
- DE LA CRUZ, R. A. L. , DIDDENS, C. , ZHANG, X. & LOHSE, D. 2021 Marangoni instability triggered by selective evaporation of a binary liquid inside a Hele-Shaw cell. *J. Fluid Mech.* **923**, A16.
- DEEGAN, R. D. , BAKAJIN, O. , DUPONT, T. F. , HUBER, G. , NAGEL, S. R. & WITTEN,

- T. A. 1997 Capillary flow as the cause of ring stains from dried liquid drops. *Nature* **389** (6653), 827–829.
- DEEGAN, R. D. , BAKAJIN, O. , DUPONT, T. F. , HUBER, G. , NAGEL, S. R. & WITTEN, T. A. 2000 Contact line deposits in an evaporating drop. *Phys. Rev. E* **62** (1), 756.
- DIDDENS, C. 2017 Detailed finite element method modeling of evaporating multi-component droplets. *J. Comput. Phys.* **340**, 670–687.
- DIDDENS, C. , KUERTEN, J. G. , VAN DER GELD, C. & WIJSHOFF, H. 2017a Modeling the evaporation of sessile multi-component droplets. *J. Colloid Interface Sci.* **487**, 426–436.
- DIDDENS, C. , LI, Y. & LOHSE, D. 2021 Competing Marangoni and Rayleigh convection in evaporating binary droplets. *J. Fluid Mech.* **914**, A23.
- DIDDENS, C. & ROCHA, D. 2024 Bifurcation tracking on moving meshes and with consideration of azimuthal symmetry breaking instabilities. *J. Comput. Phys.* **518**, 113306.
- DIDDENS, C. , TAN, H. , LV, P. , VERSLUIS, M. , KUERTEN, J. , ZHANG, X. & LOHSE, D. 2017b Evaporating pure, binary and ternary droplets: thermal effects and axial symmetry breaking. *J. Fluid Mech.* **823**, 470–497.
- DUGAS, V. , BROUTIN, J. & SOUTEYRAND, E. 2005 Droplet evaporation study applied to DNA chip manufacturing. *Langmuir* **21** (20), 9130–9136.
- EDWARDS, A. , ATKINSON, P. , CHEUNG, C. , LIANG, H. , FAIRHURST, D. & OUALI, F. 2018 Density-driven flows in evaporating binary liquid droplets. *Phys. Rev. Lett.* **121** (18), 184501.
- EGGERS, J. & PISMEN, L. M. 2010 Nonlocal description of evaporating drops. *Phys. Fluids* **22** (11).
- FUKATANI, Y. , OREJON, D. , KITA, Y. , TAKATA, Y. , KIM, J. & SEFIANE, K. 2016 Effect of ambient temperature and relative humidity on interfacial temperature during early stages of drop evaporation. *Phys. Rev. E* **93** (4), 043103.
- GELDERBLOM, H. , DIDDENS, C. & MARIN, A. 2022 Evaporation-driven liquid flow in sessile droplets. *Soft Matter* **18** (45), 8535–8553.
- GOLUBITSKY, M. & SCHAEFFER, D. 1979 A theory for imperfect bifurcation via singularity theory. *Commun. Pure Appl. Math* **32** (1), 21–98.
- HE, M. & QIU, H. 2016 Internal flow patterns of an evaporating multicomponent droplet on a flat surface. *Int. J. Therm. Sci.* **100**, 10–19.
- HEIL, M. & HAZEL, A. L. 2006 oomph-lib - an Object-Oriented Multi-Physics finite-element library. In *Fluid-structure interaction: Modelling, simulation, optimisation*, pp. 19–49. Springer.
- HOSOI, A. & BUSH, J. W. 2001 Evaporative instabilities in climbing films. *J. Fluid Mech.* **442**, 217–239.
- HU, H. & LARSON, R. G. 2002 Evaporation of a sessile droplet on a substrate. *J. Phys. Chem. B* **106** (6), 1334–1344.
- HU, H. & LARSON, R. G. 2006 Marangoni effect reverses coffee-ring depositions. *J. Phys. Chem. B* **110** (14), 7090–7094.
- KARPITSCHKA, S. , LIEBIG, F. & RIEGLER, H. 2017 Marangoni contraction of evaporating sessile droplets of binary mixtures. *Langmuir* **33** (19), 4682–4687.
- KIM, J. 2007 Spray cooling heat transfer: The state of the art. *Int. J. Heat Fluid Flow* **28** (4), 753–767.
- KITA, Y. , OKAUCHI, Y. , FUKATANI, Y. , OREJON, D. , KOHNO, M. , TAKATA, Y. & SEFIANE, K. 2018 Quantifying vapor transfer into evaporating ethanol drops in a humid atmosphere. *Phys. Chem. Chem. Phys.* **20** (29), 19430–19440.
- LI, Y. , DIDDENS, C. , LV, P. , WIJSHOFF, H. , VERSLUIS, M. & LOHSE, D. 2019 Gravitational effect in evaporating binary microdroplets. *Phys. Rev. Lett.* **122** (11), 114501.
- LINDE, H. , PFAFF, S. & ZIRKEL, C. 1964 Flow investigations into the hydrodynamic instability of liquid-gaseous phase boundaries using the capillary gap method. *J. of Phys. Chem.* **225** (1), 72–100.
- LOEWENTHAL, M. 1931 XI. tears of strong wine. *London Edinburgh Philos. Mag. & J. Sci.* **12**, 462–472.
- LOHSE, D. 2022 Fundamental fluid dynamics challenges in inkjet printing. *Annu. Rev. Fluid Mech.* **54** (1), 349–382.

- LOHSE, D. & ZHANG, X. 2020 Physicochemical hydrodynamics of droplets out of equilibrium. *Nat. Rev. Phys.* **2** (8), 426–443.
- MACHRAFI, H. , REDNIKOV, A. , COLINET, P. & DAUBY, P. 2010 Bénard instabilities in a binary-liquid layer evaporating into an inert gas. *J. Colloid Interface Sci.* **349** (1), 331–353.
- PAHLAVAN, A. A. , YANG, L. , BAIN, C. D. & STONE, H. A. 2021 Evaporation of binary-mixture liquid droplets: the formation of picoliter pancakelike shapes. *Phys. Rev. Lett.* **127** (2), 024501.
- PEARSON, J. 1958 On convection cells induced by surface tension. *J. Fluid Mech.* **4** (5), 489–500.
- POPOV, Y. O. 2005 Evaporative deposition patterns: spatial dimensions of the deposit. *Phys. Rev. E* **71** (3), 036313.
- ROWAN, S. , NEWTON, M. , DRIEWER, F. & MCHALE, G. 2000 Evaporation of microdroplets of azeotropic liquids. *J. Phys. Chem. B* **104** (34), 8217–8220.
- SEFIANE, K. , DAVID, S. & SHANAHAN, M. E. 2008 Wetting and evaporation of binary mixture drops. *J. Phys. Chem. B* **112** (36), 11317–11323.
- SHIN, S. , JACOBI, I. & STONE, H. A. 2016 Bénard-Marangoni instability driven by moisture absorption. *Europhys. Lett.* **113** (2), 24002.
- STERNLING, C. , & SCRIVEN, L. 1959 Interfacial turbulence: hydrodynamic instability and the Marangoni effect. *AIChE J.* **5** (4), 514–523.
- STROGATZ, S. H. 2018 *Nonlinear dynamics and chaos: with applications to physics, biology, chemistry, and engineering*. CRC press.
- TAN, H. , DIDDENS, C. , LV, P. , KUERTEN, J. G. , ZHANG, X. & LOHSE, D. 2016 Evaporation-triggered microdroplet nucleation and the four life phases of an evaporating Ouzo drop. *Proc. Natl. Acad. Sci.* **113** (31), 8642–8647.
- THOMSON, J. 1855 XLII. On certain curious motions observable at the surfaces of wine and other alcoholic liquors. *Philos. Mag.* **10**, 330–333.
- WANG, Z. , OREJON, D. , TAKATA, Y. & SEFIANE, K. 2022 Wetting and evaporation of multicomponent droplets. *Phys. Rep.* **960**, 1–37.
- WIESEL, W. E. 1993 Continuous time algorithm for Lyapunov exponents. *Phys. Rev. E* **47** (5), 3686.
- YANG, L. , PAHLAVAN, A. A. , STONE, H. A. & BAIN, C. D. 2023 Evaporation of alcohol droplets on surfaces in moist air. *Proc. Natl. Acad. Sci.* **120** (38), e2302653120.